Improving the Representation of Snow Crystal Properties Within a Single-Moment Microphysics Scheme

Andrew L. Molthan[1,2], Walter A. Petersen[2], Jonathan L. Case[3], and Scott R. Dembek[4]

[1]*NASA/MSFC Short-term Prediction Research and Transition (SPoRT) Center, Huntsville, AL*

[2]*Earth Science Office, NASA/MSFC, Huntsville, AL*

[3]*ENSCO, Inc. and NASA SPoRT Center, Huntsville, AL*

[4]*Universities Space Research Association/NASA SPoRT, Huntsville, AL*

1. INTRODUCTION AND BACKGROUND

As computational resources continue their expansion, weather forecast models are transitioning to the use of parameterizations that predict the evolution of hydrometeors and their microphysical processes, rather than estimating the bulk effects of clouds and precipitation that occur on a sub-grid scale. These parameterizations are referred to as single-moment, bulk water microphysics schemes, as they predict the total water mass among hydrometeors in a limited number of classes. Although the development of single-moment microphysics schemes have often been driven by the need to predict the structure of convective storms, they may also provide value in predicting accumulations of snowfall.

Predicting the accumulation of snowfall presents unique challenges to forecasters and microphysics schemes. In cases where surface temperatures are near freezing, accumulated depth often depends upon the snowfall rate and the ability to overcome an initial warm layer. Precipitation efficiency relates to the dominant ice crystal habit, as dendrites and plates have relatively large surface areas for the accretion of cloud water and ice, but are only favored within a narrow range of ice supersaturation and temperature. Forecast models and their parameterizations must accurately represent the characteristics of snow crystal populations, such as their size distribution, bulk density and fall speed. These properties relate to the vertical distribution of ice within simulated clouds, the temperature profile through latent heat release, and the eventual precipitation rate measured at the surface.

The NASA Goddard, single-moment microphysics scheme is available to the operational forecast community as an option within the Weather Research and Forecasting (WRF) model. The NASA Goddard scheme predicts the occurrence of up to six classes of water mass: vapor, cloud ice, cloud water, rain, snow and either graupel or hail. Exponential size distributions are used for the precipitating hydrometeor classes of rain, snow and graupel following Marshall and Palmer (1948) and Gunn and Marshall (1958), while cloud ice and water categories are assumed to be monodisperse. Although the bulk of the simulated physical processes are based upon Lin et al. (1983) and Rutledge and Hobbs (1983), the NASA Goddard scheme includes several modifications

that include new saturation adjustment schemes, changes to graupel source and sink terms, and treatment of microphysical processes based upon a single thermodynamic profile (Tao et al. 2003; Lang et al. 2007). The NASA Goddard scheme has been compared against similar WRF model schemes and shown to produce comparable structures for mesoscale convective systems and tropical cyclones (Tao et al. 2008).

2. DATA AND METHODOLOGY

Although the NASA Goddard scheme has demonstrated value when simulating the structure of tropical or midlatitude convection (Tao et al. 2008), there have been fewer opportunities to compare predictions and observations of snowfall. The success of the NASA Goddard scheme hinges upon an ability to represent the size distribution, bulk density, and fall speeds of snow crystals, as their simulated interactions with other species determine the vertical distribution of water and ice mass, or precipitation. The Canadian CloudSat/CALIPSO Validation Project (C3VP) provides a unique opportunity to validate the assumptions and performance of the NASA Goddard scheme when simulating the widespread snowfall associated with the passing of an extratropical cyclone. Aircraft and surface observations provide the data required to validate many assumptions related to snowfall within the NASA Goddard scheme. The availability of CloudSat and an operational, C-band weather radar provide remote sensors for additional evaluation. This event can be used to evaluate the performance of the NASA Goddard scheme, and to develop alternative parameterizations to improve upon poor assumptions, if required.

a. Particle Size Distributions from Aircraft

An instrumented aircraft (NRC Convair-580) measured atmospheric state variables and snow crystal size distributions as it maneuvered through spiral trajectories, climbs and descents in the vicinity of the dual-polarimetric, C-band radar system located near King City, Ontario. The King City radar was supplemented by a descending pass of the CloudSat radar, which sampled cloud profiles representative of precipitation that occurred across the C3VP domain. Aircraft instrumentation provided a vertical profile of size

distribution parameters, required for the validation of assumptions regarding snow crystals that are commonly made within a single-moment, bulk water microphysics scheme. In addition, these data sets can be used to validate the model simulation of ice water content and radar reflectivity.

The Convair-580 aircraft was equipped with Particle Measuring Systems (PMS) 2D-C (15 μm-0.96 mm) and 2D-P (0.2-6.4 mm) imaging probes capable of measuring both crystal diameters and number concentration. Crystal imagery provide evidence of crystal habit and the onset of aggregation, with particle dimension measured by their single dimension projection. Crystal probe data were post-processed by A. Heymsfield (personal communication) to produce a unified set of size distributions that accommodate the overlap in size range of the 2D-C and 2D-P systems.

Aircraft measurement of ice crystal size distributions offer a unique opportunity to validate key assumptions within the NASA Goddard scheme: the use of a fixed, exponential distribution intercept, and the use of a fixed bulk density to describe all populations of snow crystals. The moment fitting method of Heymsfield et al. (2002) can be applied to estimate distribution parameters, but care must be taken in the application of size distributions measured directly by the aircraft probes. Heymsfield et al. (2008) discussed the problems of large crystals shattering upon impact with the probe housings, contributing to inflated numbers of small crystals. These small, shattered remnants do not accurately represent the natural characteristics of crystal populations, and adversely affect distribution parameters. Although methods can identify shattered crystal remnants and exclude them from the analysis (Field et al. 2006), the necessary data were not immediately available. Instead, particles less than 60 μm were neglected in aircraft data analyses.

Once these small crystals were elimianted, the moment fitting method of Heymsfield et al. (2002) was used, where the first and second moments of the measured size distribution uniquely determine the slope and intercept of an exponential size distribution. Parameters for the moment-fit, exponential size distribution were retained if they produced an $R^2 \geq 0.8$ when compared against observations. The inclusion of a counterflow virtual impactor (CVI, Twohy et al. 1997) provided in-flight measurement of total ice or liquid water content and an estimate of the population effective bulk density (Heymsfield et al. 2004) by dividing the CVI estimated value by the total volume of equivalent diameter spheres represented within each best-fit size distribution.

b. Simulation with the WRF Model and NASA Goddard Microphysics Scheme

On 22 January 2007, an extratropical cyclone produced an extensive area of light to moderate snowfall across the Great Lakes and southern Ontario, which was sampled by a suite of direct and remote sensors available to the C3VP campaign. This event was well-simulated using the WRF model in a triply nested configuration at 9, 3 and 1 km, using half-degree analyses from the NCEP Global Forecast System (GFS) as boundary conditions (Shi et al. 2009).
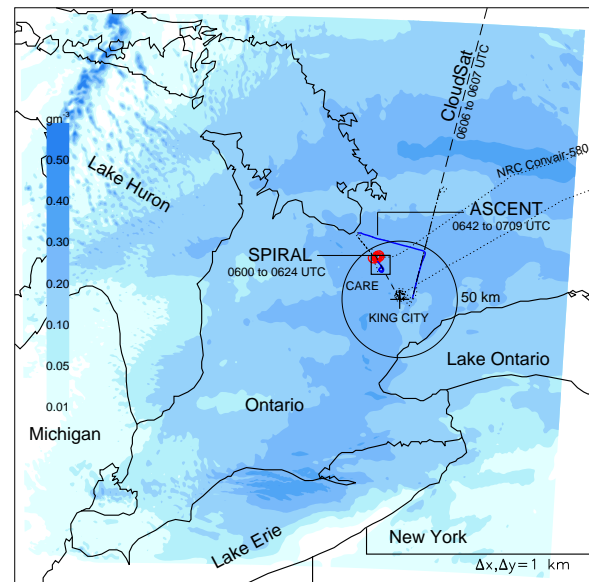

Fig. 1. Snow content at the lowest altitude model vertical level, valid at 0600 UTC on 22 January 2007, based upon initial and boundary conditions from the NCEP GFS model and the NASA Goddard single-moment microphysics scheme. Location of C3VP campaign assets are indicated: the Canadian Center for Atmospheric Experiments (CARE), the King City radar, the CloudSat flight track, and the flight track of the NRC Convair-580 aircraft. Aircraft data segments used here are indicated as the descending spiral and departure ascent in the vicinity of the King City radar.

Here, the same triply-nested grid configuration is utilized with physical parameterizations to mirror the configuration of experimental forecasts produced by the National Severe Storms Laboratory (Table 1 and Kain et al. 2008). Within the highest resolution domain, the resulting forecast depicts the widespread nature of the synoptic-scale snowfall event, along with isolated areas of enhanced snow content. Since the WRF model forecast provides a reasonable simulation of the actual event, comparisons can be made between model assumptions, profiles of hydrometeor content, and observations from C3VP data (Figure 1)

3. EVALUATION OF MODEL VERTICAL PROFILES

Variability among the model grids was evaluated by examining vertical profiles of key parameters, averaged among grid points nearest the CARE site. Due to the consistent, nested forcing applied to the three domains, vertical profiles of hydrometeor content, moisture and temperature are practically identical when averaged over numbers of grid cells equivalent to the spatial area of the 9 km grid point (Figure 2). Mean profiles of ice water content fell within the range of aircraft observations, considering that the aircraft CVI includes a 10 to 20% error and measures a mass equivalent to the combination of cloud ice and snow predicted by the NASA Goddard scheme (Figure 2a). Aircraft data sampled discrete layers of enhanced ice water content near altitudes of 1 and 2 km that were not represented in the model vertical profile. These layers of enhanced IWC may be the result of earlier seeder-feeder processes or other processes operating on vertical scales not represented by the model

Table 1. Configuration of the WRF model for simulation of the 22 January 2007 snowfall event, following Shi et al. (2009).

Physical Process	Parameterization Scheme	Notes
Boundary Layer	Mellor-Yamada-Janjic	Janjić (1990, 1996, 2002)
Longwave Radiation	Rapid Radiative Transfer	Mlawer et al. (1997)
Shortwave Radiation	Dudhia Scheme	Dudhia (1989)
Land Surface Processes	NOAH Land Surface Model	Ek et al. (2003)
Cloud Microphysics	NASA Goddard Scheme	Tao et al. (2008)
9 km Cumulus Parameterization	Grell-Devenyi Scheme	Grell and Devenyi (2002)
Saturation Adjustment	NASA Goddard Scheme	Tao et al. (2003)

resolution. Although the simulation of graupel is permitted in the NASA Goddard scheme, no significant amounts of graupel were predicted in the vicinity of the CARE site, coincident with crystal probe imagery where distinct habits were still visible.

Profiles of water vapor, presented in terms of saturation with respect to water and ice, only differ with minor decreases in low level saturation at increasing horizontal resolution (Figure 2b). All forecasts sublimate precipitating ice and evaporate cloud water to restore saturation. Above the 3.5 km level there are sharp differences between the model and observations due to the particular saturation adjustment scheme chosen for this simulation. In this forecast, a temperature threshold of -15^oC determines whether saturation adjustment will occur with respect to water or ice. In this case, at temperatures colder than -15^oC, excess vapor is deposited to the cloud ice category with a corresponding warming associated with latent heat release. This may contribute, at least in part, to the warm bias observed throughout much of the temperature profile, and specifically in the 3-4 km level where the abrupt departure is noted (Figure 2c).

4. EVALUATION OF PARTICLE SIZE DISTRIBUTIONS AND BULK DENSITY

Given that the model forecast reasonably depicts the spatial coverage and intensity of precipitation, attention turns to the validity of assumptions within the NASA Goddard scheme related to snow crystal size distributions and their bulk density. Mean profiles of the snow distribution slope parameter (λ) were obtained for WRF model profiles within a 50 km radius of the King City radar location (Figure 3). Below 3 km, the simulated mean profile of λ overestimates aircraft estimated values, implying that the model forecast produced a size distribution with mean sizes smaller than observed. The ascending aircraft profile demonstrates a smooth decrease in λ with height and is presumed to be representative of the broader precipitation shield, with λ approaching 1 mm^{-1} near cloud base, a value comparable to the minimum in a summary parameterization by Ryan (2000). Instead, the NASA Goddard scheme produced an asymptotic value near 2 mm^{-1} through a depth of 3 km.

The best fit between aircraft estimations of λ and model calculations was obtained when the simulated cloud ice and snow are combined and included as ice water content, and the model value of λ is calculated using the fixed intercept (N_{os}) and density (ρ_s). At altitudes above 3 km, the NASA Goddard scheme produced a reasonable ice water content and distribution slope parameter, but incorrectly assumed that the ice crystals could be represented by monodisperse, pure ice spheres. The scheme would benefit by smoothing the transition between these categories. In summary, the NASA Goddard scheme predicted a reasonable ice water content but incorrectly assumed that crystals near cloud top were significantly different from those at lower altitudes.

In the case of the distribution intercept (N_{os}), the use of a constant value fails to represent the diversity among aircraft samples and does not represent the general decrease in N_{os} toward cloud base. Aircraft measurements span two orders of magnitude, while the use of a constant represents conditions only near the 3 km level. In addition, estimates of the snow bulk density (ρ_s) suggest that the value of 100 $kg\ m^{-3}$ assigned to snow in the NASA Goddard scheme was rarely observed. Instead, density decreases toward cloud base in a manner similar to the slope parameter. Heymsfield et al. (2004) demonstrated this relationship and noted that a constant density is not representative of the natural environment.

5. EVALUATION OF THE SNOW TERMINAL VELOCITY-DIAMETER RELATIONSHIP

The Hydrometeor Velocity and Shape Detector Barthazy et al. (2004) was available at the C3VP site, and uses digital imagery to track individual snow crystals in order to estimate their dimension and fall speed. In this case, it is assumed that the measured speed is the terminal velocity, and a joint histogram of diameter and fall speed was constructed (Figure 4). Best-fit, power-law relationships were developed following the form of Locatelli and Hobbs (1974), in order to compare C3VP observations to previously published relationships and equations used within the NASA Goddard scheme. The resulting relationship from C3VP data was very similar to observations of aggregates obtained by Locatelli and Hobbs (1974), while the equation in the current NASA Goddard scheme produced fall speeds that were too low across the full range of crystal diameters.

Despite an underestimation of particle fall speeds, modeled surface precipitation rates were reasonable when compared against data at the CARE site (Figure 4). Precipitation rates are sensitive to the terminal velocity relationship, mass-diameter relationship (density) and the mean size of particles within the simulated size distribution. Given that the current equation used by the NASA Goddard scheme underestimates particle fall speeds, adjustment of the fall speed equation and size distributions to C3VP observations will increase snowfall precipitation rates and may degrade one component of the forecast while improving the representation of snow crystals within the model vertical column.
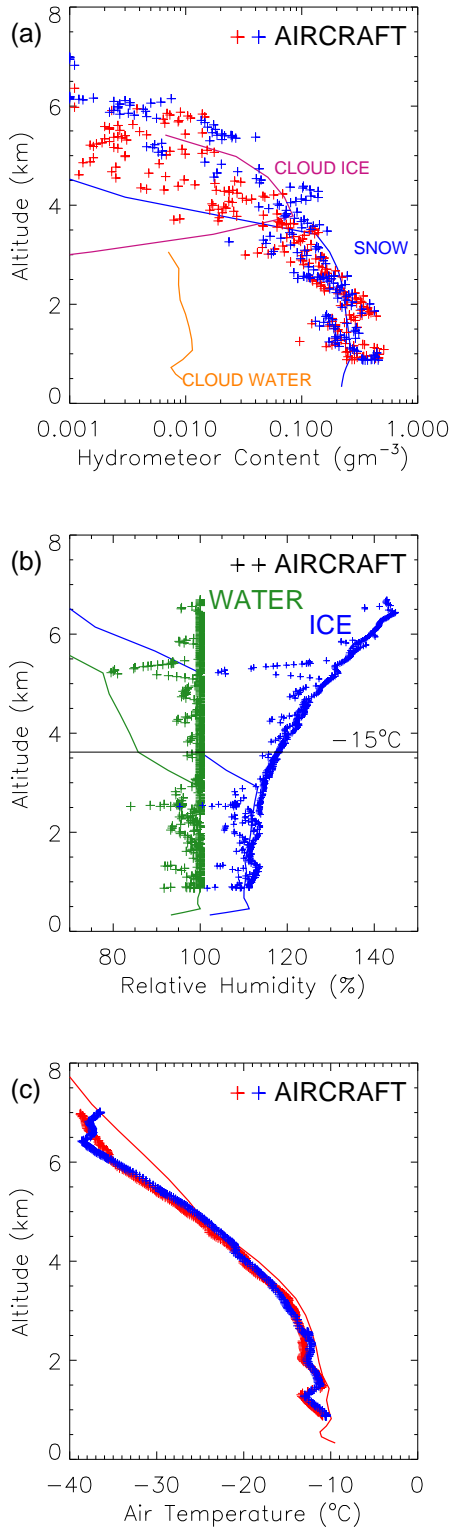
Fig. 2. Comparisons of model vertical profiles among grids with varying spatial resolutions. (a) Mean profile of hydrometeor content for the model grid point nearest the CARE site, compared with aircraft profile estimates of ice water content. (b) Vertical profiles of saturation with respect to water (green) and ice (blue) compared to aircraft spiral data. (c) Profile of air temperature. Colors of aircraft data symbols are repeated from Figure 1.

Table 2. Series of modifications to the NASA Goddard scheme in an experimental forecast implementing changes in snow crystal terminal velocities, $\lambda(T)$ and $\rho_s(\lambda)$.

Model Parameter	Equation	Unit
$\lambda(T)$	$851.617 \times 10.0^{-0.031 T_c}$	m^{-1},T^{o}C
$\rho_s(\lambda)$	$0.241 \lambda^{0.722}$	$kg\ m^{-3}$
(a_v, b_v)	$(110.083, 0.145)$	$(cm^{1-b_v}\ s^{-1})$

6. DEVELOPMENT AND EVALUATION OF A TEMPERATURE-BASED PARAMETERIZATION

In an analysis of several field campaigns around the globe, Ryan (2000) developed an equation that was broadly representative of the monotonic relationship between the slope parameter λ and temperature. The parameterization of $\lambda(T)$ was applied to populations of snow crystals larger than 100 μm and fit to an exponential size distribution. Since the NASA Goddard scheme also uses an exponential size distribution for snow, an examination of a $\lambda(T)$ approach is pursued.

In Figure 5, a scatterplot of air temperature and λ demonstrates that the C3VP aircraft observations are comparable to the equation proposed by Ryan (2000), although the best-fit equation specific tot he C3VP data offers a slight improvement as measured by the R^2 value. The value of λ will be overestimated by $\lambda(T)$ at the warmest temperatures (near cloud base), as cluttering of observed λ occurs in the -10° to -15^oC region due to a nearly isothermal temperature profile.

Variability in the snow bulk density can be accommodated by incorporating a parameterization suggested by Heymsfield et al. (2004), who used a power-law fit of $\rho_s = a\lambda^b$, based upon ice crystals accumulated in anvil outflows and frontal clouds. A scatterplot of C3VP aircraft observations for λ and ρ_s are scattered around the relationship proposed by Heymsfield et al. (2004). Paired observations of λ and ρ_s are dominated by contributions from small values of λ, but a parameterization must represent a broad sampling of values. Therefore, a best-fit line was constructed for mean values of ρ_s over small increments of λ, allowing for densities to range from 20 to 100 $kg\ m^{-3}$ (Figure 5b). The combined parameterizations of the size distribution slope and density incorporate two, new components of variability that were previously unavailable within the NASA Goddard scheme. This configuration leaves the distribution intercept (N_{os}) to be calculated through conservation of snow mass, as predicted by the microphysical processes within the NASA Goddard scheme. In addition to functional fits for the distribution slope and bulk density, the terminal velocity-diameter relationship has been modified to fit surface observations from the HVSD system located at the C3VP site (Figure 4 and Table 2).

a. Evaluation

By repeating the same forecast with new parameterizations, the result is an experimental forecast that can be compared against the results of the original, or control NASA Goddard scheme. Spatial patterns of snowfall were comparable with a slight increase in the predicted storm
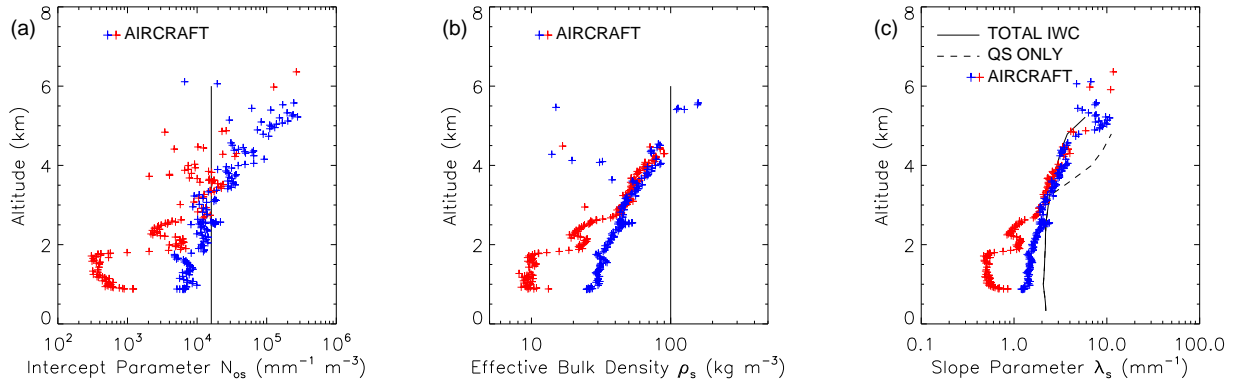
Fig. 3. Mean vertical profiles of snow crystal size distribution parameters and density, compared to model output near the King City radar. Vertical lines represent the fixed values used within the NASA Goddard scheme. (a) Distribution intercept parameter. (b) Snow bulk density. (c) Distribution slope parameter.
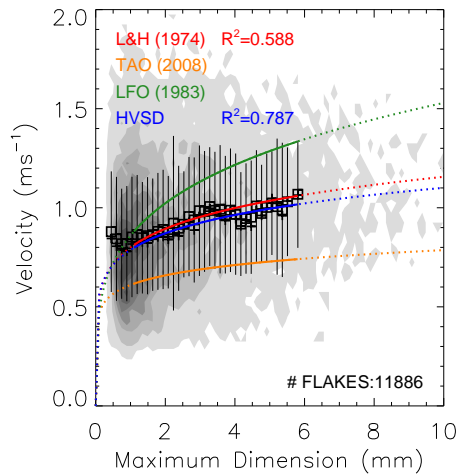

Fig. 4. Joint histogram of crystal maximum dimension and HVSD estimate of terminal fall speed along with proposed fits by Locatelli and Hobbs (1974), Lin et al. (1983) and Tao et al. (2008). The R^2 value derived from relationships other than Locatelli and Hobbs (1974) are omitted as they do not represent observations. Mean (crosshair), median (open square) and standard deviation of terminal velocities are plotted for each size bin where data were sufficient ($N \geq 50$) for providing a best fit estimate. Relationships are extrapolated for sizes smaller than 1 mm and less than 50 occurrences (dashed). Histogram shading is performed at 1%, 10% and every 10% thereafter.

total, liquid equivalent precipitation at the CARE site. As in the control forecast, profiles of ice water content, size distribution parameters and bulk density were extracted for a 9 km square region centered on the King City radar location.

Through the use of a temperature-based parameterization, the slope parameter $\lambda(T)$ is adjusted to slightly lower values in the lowest 3 km (Figure 6a). This change allows for a continued decrease in the predicted λ as crystal populations approach the surface, but the nearly isothermal character of the temperature profile prohibits a continued decrease in λ as observed by aircraft data. At altitudes above 3 km, the model profile is dominated by monodisperse cloud ice,

although the predicted value of $\lambda(T)$ is comparable to aircraft observations of exponential size distributions. The parameterization of $\lambda(T)$ contributes to increased variability in λ, as observed in aircraft data, and would be suitable for representing size distributions near cloud top if the cloud ice category included a complete size distribution.

The portrayal of bulk density is improved by incorporating a dependence upon λ, as proposed by Heymsfield et al. (2004), although accurate prediction of ρ_s is dependent upon the prediction of λ by temperature. Inclusion of $\rho_s(\lambda)$ allows for greater flexibility over the fixed value approach and allows for a decrease in bulk density toward cloud base, although density values stagnate as the temperature profile becomes nearly isothermal and variability in $\lambda(T)$ decreases (Figure 6). Through a conservation of mass calculation, the profile of the distribution intercept (N_{os}) is improved over the fixed value approach and does a better job of representing the observed increase in N_{os} with altitude. Errors in $\lambda(T)$ and the subsequent calculation of ρ_s contribute to errors in the prediction of N_{os} resulting in an underestimate (overestimate) of the distribution intercept near cloud base (cloud top) (Figure 6c).

Although a temperature dependent approach has merit, its success is limited in regions where the temperature profile exhibits little variability. Instead, populations of ice crystals continue to evolve with decreasing altitude as they grow, aggregate and precipitate. New parameterizations must be able to incorporate this steady evolution, and temperature dependence may be ineffective at low levels where inversions or isothermal layers occur in the presence of warm air advection.

7. DEVELOPMENT AND EVALUATION OF A COLUMN-INTEGRATED PARAMETERIZATION

The properties of snow crystals sampled by the aircraft exhibit consistent changes with height as cloud top crystals grow, precipitate, aggregate, and reach the surface. Although the temperature profile can be used as a proxy for altitude, use in parameterization is complicated in this case by inversions and a deep, nearly isothermal layer. As an additional
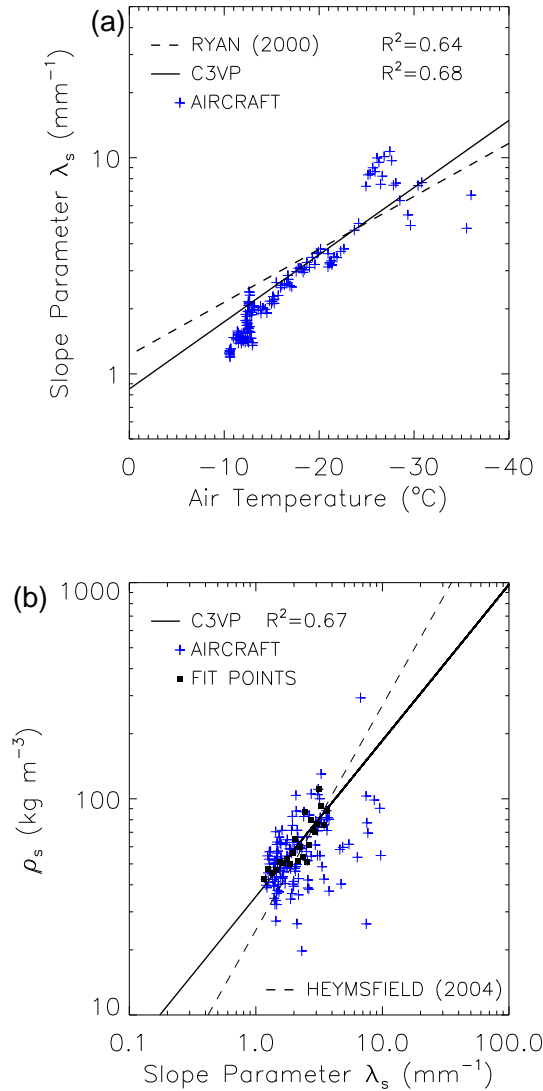
Fig. 5. (a) Scatterplot of the slope parameter (λ) and air temperature, obtained from C3VP aircraft instrument probe data, along with best-fit equation in Table 2 and the parameterization suggested by Ryan (2000). (b) Scatterplot of the distribution slope parameter (λ) and effective snow bulk density (ρ_s), with best fit line to means of C3VP data, in comparison to the parameterizations of Heymsfield et al. (2004).

Table 3. Series of modifications to the NASA Goddard scheme in an experimental forecast implementing changes in snow crystal terminal velocities, $\lambda(EXCP)$ and $\rho_s(\lambda)$.

Model Parameter	Equation	Unit
$\lambda(EXCP)$	$3605.9e^{-2.2 \times EXCP} + 722.2$	$m^{-1}, kg\ m^{-2}$
$\rho_s(\lambda)$	$0.241\lambda^{0.722}$	$kg\ m^{-3}$
(a_v, b_v)	$(110.083, 0.145)$	$(cm^{1-b_v}\ s^{-1})$

top to base and defined as the excess vapor path (EXCP), linked to the distribution slope parameter with an exponential function. The parameterization of $\rho_s(\lambda)$ is retained from the first experiment, along with changes to the terminal velocity-diameter relationship.

a. Evaluation

The column integrated approach improves the representation of the slope parameter by allowing for a continuous decrease in λ toward cloud base, while the parameterization of $\lambda(T)$ was impacted by the isothermal nature of the low level temperature profile. There is a slight underestimation of λ values observed by aircraft, but the increase in λ from cloud base to top is better represented than in the control experiment or $\lambda(T)$ approach (Figure 8a). Consistent with an improved representation of λ, the snow bulk density achieves a closer fit to observations in the lowest 3 km, with success limited by the large amount of scatter in the original λ and ρ_s best-fit relationship (Figure 8b). When combined, the slight underestimation of λ and overestimate of ρ_s contribute to a general underestimation of N_{os}, although the steady increase in the distribution intercept is well represented within the forecast (Figure 8c). This second experiment demonstrates that variability in distribution parameters with height can be represented with a column-based approach that incorporates temperature as one piece of information, but the specific relationship for $\lambda(EXCP)$ will likely vary among clouds of different depth and ice crystal habit, or degree of aggregation, and therefore this result is limited to one particular case. Instead, future parameterizations could include adaptation of a parameter that describes ice crystal properties as functions of temperature and ice saturation (habit) as well as their time spent within the cloud, where they will continue to grow and aggregate, leading to decreases in λ and ρ_s while increasing ice water content.

8. APPLICATION OF RADAR REMOTE SENSING IN MODEL EVALUATION

High resolution forecast models predict the hydrometeor contents for varying number of species, which result in vertical profiles of water or ice mass, assumed to be distributed among a range of sizes. Radars are sensitive to precipitation mass and size distribution through an accumulation of radar backscatter, which has been used previously by Lang et al. (2007) to evaluate the NASA Goddard scheme. During the 22 January 2007 event, precipitation was observed by the C-band, dual-polarimetric radar at King City, Ontario as well as the CloudSat Cloud Profiling Radar (Figure 9). Calculation of
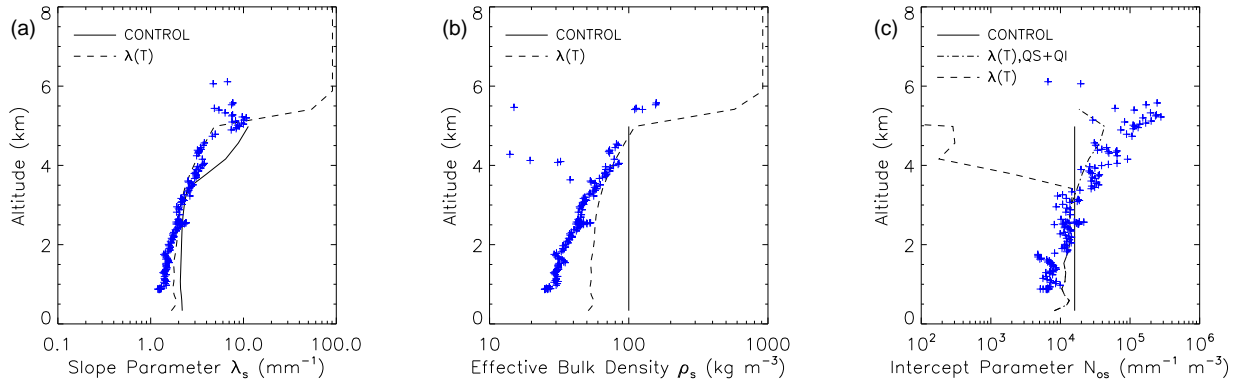
experiment, a column-integrated approach was used that incorporates information from the temperature profile but allows for a steadily increasing parameter that provides a functional fit to snow crystal properties. Ice crystal habits are sensitive to both temperature and the degree of ice supersaturation, and a column integration of the excess vapor with respect to ice is utilized with functional relationships to the distribution slope parameter (Figure 7 and Table 3). Although the current NASA Goddard scheme does not include any type of habit prediction or calculations specific to crystal types, calculation of excess vapor pressure may facilitate other experiments in the future. Here, the excess vapor with respect to ice saturation is summed from cloud

Fig. 6.   As in Figure 3 but based upon the results from the NASA Goddard scheme, utilizing a parameterization with $\lambda(T)$ and $\rho_s(\lambda)$, and fall speed relationship in Figure 4. Relationship equations are listed in Table 2.
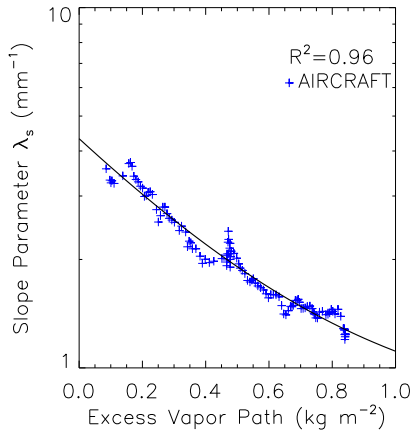

Fig. 7.   Scatterplot of excess vapor path with respect to ice and aircraft estimates of the slope parameter, along with best-fit line and goodness of fit estimate, R^2.

a radar reflectivity from simulated snowfall can be obtained by assuming Rayleigh scattering from equivalent diameter, pure ice spheres in the case of the King City radar (Smith 1984), but due to the diverse scattering characteristics of true ice crystal shapes (Liu 2004, 2008), simulation of CloudSat reflectivity is more complex. Although the model assumes a spherical shape, simulated snow crystals are represented as low density aggregates with single-scattering properties obtained from the fractal aggregates described by Ishimoto (2008). The use of low density aggregates from Ishimoto (2008) is appropriate, based upon crystal probe imagery that indicate a dominance of aggregates (not shown) and a mass-diameter relationship similar to the summary equation in Heymsfield et al. (2004).

In Figure 10a, the median profile of King City radar reflectivity is shown, based upon a 0555 UTC volume scan with 50 km radius. The reflectivity profile is asymptotic within the lowest 2 *km*, with values near 20 dBZ. In the control forecast, the median profile of King City radar reflectivity was well-

represented, although the size distribution and bulk densities did not represent aircraft observations. When a temperature-based parameterization is utilized, the forecast improves the representation of snow properties while retaining a reasonable fit to King City reflectivity observations. Note that there is some loss of radar reflectivity due to an overall increase (decrease) in precipitation rate (profile ice water content), but the profile shapes are comparable. The profile obtained from the $\lambda(EXCP)$ forecast provides the best match to King City radar data, except that reflectivity is overestimated in the lowest 2 *km* and fails to achieve an asymptotic shape. This error is due to the constant increase (decrease) in EXCP, which contributes to steady increases (decreases) in the mean particle size (λ) and greater number concentrations of large particles. Although the $\lambda(EXCP)$ approach improves the representation of distribution parameters and bulk density, the tail of the exponential distribution contributes to an excessively large number of large aggregates.

Comparisons of CloudSat reflectivity profiles are based upon radar returns shown in Figure 9, obtained from snowfall occurring to the north of the CARE site around 0600 UTC. The median profile of CloudSat reflectivity is similar in shape to data from the King City radar, with a steady increase in dBZ toward the surface. When reflectivity is simulated from Mie spheres (Figure 10b), the control forecast produces a uniform 7-8 dBZ in the lowest 3 *km*, coincident with the stagnation of profile values of λ. As size distribution parameters are adjusted toward observations, or as simulated values of λ decrease and represent populations of larger crystals, reflectivity from Mie spheres decreases due to resonance effects that begin at diameters beyond 0.9 *mm* (Lhermitte 1990). This effect is enhanced in the case of $\lambda(EXCP)$, since the prediction of by $\lambda(EXCP)$ provided the smallest values of simulated λ and populations of crystals with the largest mean size.

When CloudSat reflectivity is simulated from aggregates, the model forecast can replicate the increase in reflectivity from cloud top toward cloud base and demonstrate impacts from the various parameterization experiments (Figure 10c). In the control forecast, the limited range for simulated
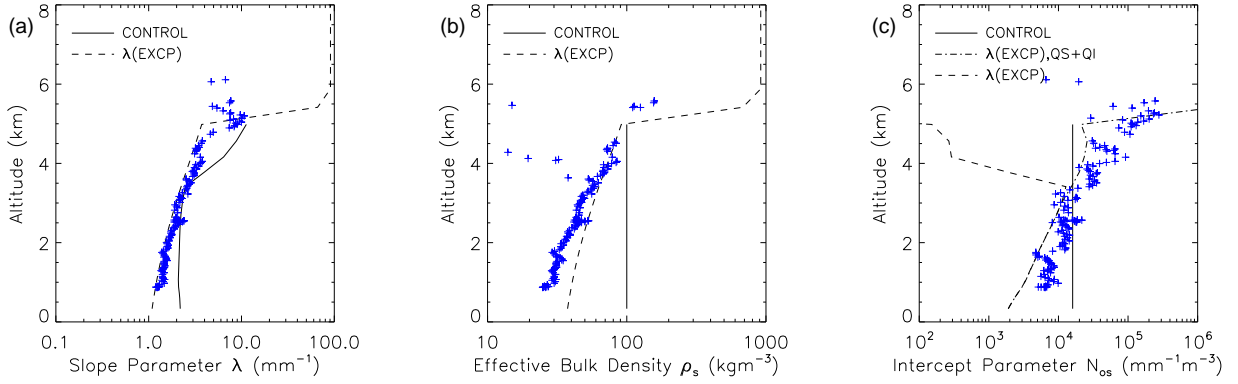
Fig. 8. As in Figure 3 but based upon the results from the NASA Goddard scheme, utilizing a parameterization with $\lambda(EXCP)$ and $\rho_s(\lambda)$, and fall speed relationship in Figure 4. Relationship equations are listed in Table 2.
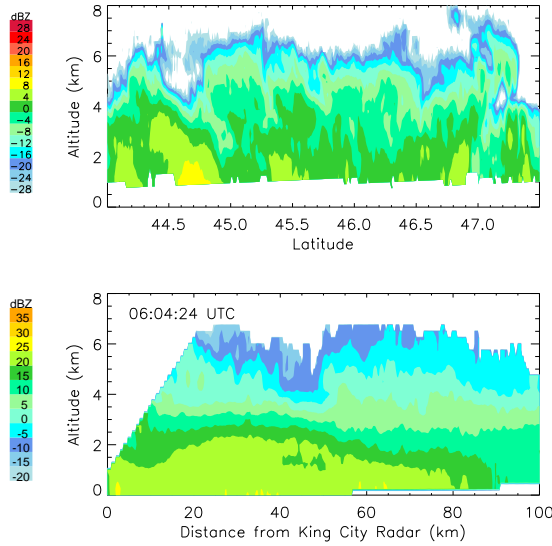

Fig. 9. (Top) Radar reflectivity profiles from the CloudSat 94 GHz Cloud Profiling Radar, obtained along the orbital segment shown in Figure 1. (Bottom) Radar reflectivity cross section along the heavily dashed line in Figure 1, obtained over the CARE site from the C-band, dual-polarimetric radar at King City, Ontario.

values of λ generate mean sizes of aggregates that are smaller than observations, while failing to represent the continued, downward decrease in λ (increase in mean size) toward cloud base. Although the use of $\lambda(T)$ offered a slight adjustment toward aircraft observations, it was not able to mimic the steady decrease in λ from aggregation effects since the simulated temperature profile was nearly isothermal. Since the profile of $\lambda(EXCP)$ provided the best representation of aircraft observations, including the steady downward decrease in λ, the column-integrated approach is able to simulate larger particles near the surface. In the parameterizations of aggregates by Ishimoto (2008), backscatter from aggregates generally increases with size. In the case of $\lambda(EXCP)$, the simulated profile of CloudSat

reflectivity continues to increase as populations with larger mean sizes (smaller λ) contribute additional backscatter. This allows for a similar lapse rate in dBZ among the CloudSat and $\lambda(EXCP)$ profiles, suggesting that the experiment with EXCP improves upon the representation of snow crystal properties, as evaluated from the W-band radar. The persistent bias in the simulated CloudSat profile is likely due to assumptions of simulated aggregates that differ from naturally occurring crystals.

9. SUMMARY AND CONCLUSIONS

Cloud microphysics schemes continue to be developed for use in high resolution, real-time forecasts and will be valuable in predicting cold-season precipitation. The size distribution and density assumptions of the NASA Goddard scheme were evaluated using the WRF model and observations obtained during the C3VP campaign for a synoptic-scale snowfall event in southern Ontario. The use of fixed constants for the snow crystal size distribution and bulk density are incapable of representing the vertical variability of each parameter, and also contribute to errors in the distribution slope parameter, which relates to the mean size of crystals within each grid volume. Two approaches were explored to improve upon the use of fixed values: an equation that uses a function of air temperature, and one that uses a column integrated value of vapor excess with respect to ice. Although both approaches provided a better fit to aircraft data, the temperature-based approach was adversely affected by the nearly isothermal nature of the low level temperature profile. In portions of the profile where the temperature variations are small, a temperature dependent equation cannot represent the continued decrease in λ due to the aggregation of individual crystals, and subsequently, is limited in its ability to represent $\rho_s(\lambda)$. A column based approach has the benefit of representing the location of crystals within the vertical, and although the parameter explored here may be less than ideal, it serves the purpose of avoiding complex shapes of the temperature profile while still incorporating temperature as a key variable. Additional cases must be
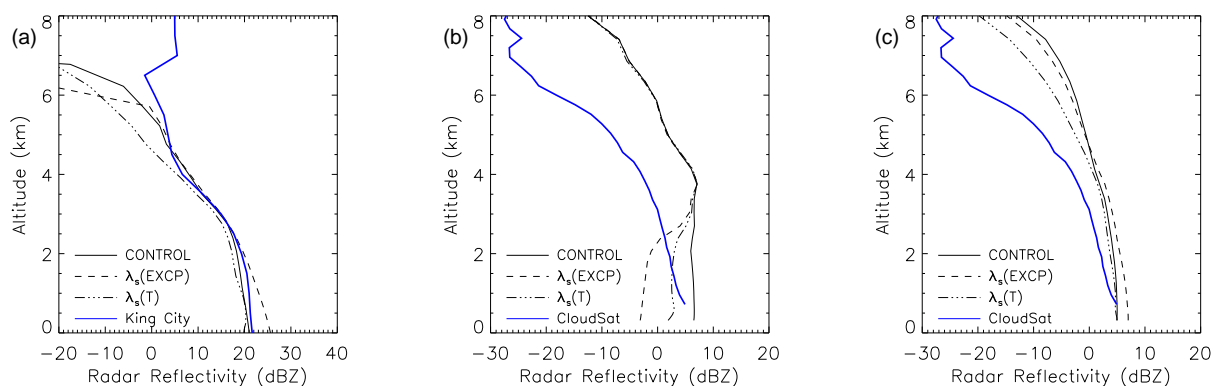
Fig. 10. Summary of various radar reflectivity profiles obtained from observations, control and experimental NASA Goddard scheme forecasts. (a) Reflectivity from the King City, Ontario radar simulated with equivalent diameter, pure ice spheres. (b) Reflectivity from CloudSat simulated from Mie scattering spheres. (c) Reflectivity from CloudSat simulated with properties of aggregates from Ishimoto (2008).

explored to determine whether a single function of $\lambda(EXCP)$ can be broadly applied to clouds of varying depth and phase.

Radar remote sensing was also applied in an evaluation of model performance. Reflectivity distributions from the C-band radar at King City, Ontario were comparable to the default configuration of the NASA Goddard scheme, although the scheme was incapable of representing the vertical variability of snow crystal properties. Other parameterizations improved upon the representation of snow properties while retaining a generally good fit to King City radar observations. In the case of CloudSat, it was shown that Mie scattering spheres will provide a poor representation of radar backscatter. Even as simulated size distributions and snow bulk densities are improved, reflectivity from Mie spheres decreases due to larger particle sizes and resonance effects. Instead, simulation of CloudSat reflectivity from aggregates will create a vertical profile that is comparable to CloudSat observations and continues to demonstrate that either the $\lambda(T)$ or $\lambda(EXCP)$ approach will improve the representation of simulated snow crystal properties while maintaining a good fit to radar observations.

ACKNOWLEDGMENTS

REFERENCES

Barthazy, E., S. Goke, R. Schefold, and D. Hogl, 2004: An optical array instrument for shape and fall velocity measurements of hydrometeors. *Journal of Atmospheric and Oceanic Technology*, **21**, 1400–1416.

Dudhia, J., 1989: Numerical study of convection observed during the winter monsoon experiment using a mesoscale two-dimensional model. *Journal of Atmospheric Sciences*, **46**, 3077–3107.

Ek, M., M. E. Mitchell, Y. Lin, E. Rogers, P. Grunmann, V. Koren, G. Gayno, and J. D. Tarpley, 2003: Implementation of NOAH land surface model advances in the National Centers for Environmental Prediction operational mesoscale Eta model. *Journal of Geophysical Research*, **108**.

Field, P. R., A. J. Heymsfield, and A. Bansemer, 2006: Shattering and particle interarrival times measured by optical array probes. *Journal of Atmospheric and Oceanic Technology*, **23**, 1357–1371.

Grell, G. A. and D. Devenyi, 2002: A generalized approach to parameterizing convection combining ensemble and data assimilation techniques. *Geophysical Research Letters*, **29**, D00A09, doi:10.1029/2007JD009766.

Gunn, K. L. S. and J. S. Marshall, 1958: The distribution with size of aggregate snowflakes. *Journal of the Atmospheric Sciences*, **15**, 452–461.

Heymsfield, A., A. Bansemer, P. Field, S. Durden, J. Stith, J. Dye, W. Hall, and T. Grainger, 2002: Observations and parameterizations of particle size distributions in deep tropical cirrus and stratiform precipitating clouds: Results from in situ observations in TRMM field campaigns. *Journal of Atmospheric Sciences*, **59**, 3457–3491.

Heymsfield, A., A. Bansemer, C. Schmitt, C. Twohy, and M. Poellot, 2004: Effective ice particle densities derived from aircraft data. *Journal of Atmospheric Sciences*, **61**, 982–1003.

Heymsfield, A. J., P. Field, and A. Bansemer, 2008: Exponential size distributions for snow. *Journal of the Atmospheric Sciences*, **65**, 4017–4031.

Ishimoto, H., 2008: Radar backscattering computations for fractal-shaped snowflakes. *Journal of the Meteorological Society of Japan*, **86**, 459–469.

Janjić, Z. I., 1990: The step-mountain coordinate: Physical package. *Monthly Weather Review*, **118**, 1429–1443.

Janjić, Z. I., 1996: The surface layer in the NCEP Eta model. *Preprints, 11th Conference on Numerical Weather Prediction, American Meteorlogical Society, Norfolk, VA*.

Janjić, Z. I., 2002: Nonsingular implementation of the Mellor-Yamada level 2.5 Scheme in the NCEP Meso model. *NCEP*

Office Note, 61, 437.

Kain, J. S., et al., 2008: Severe weather forecast guidance from the first generation of large domain convection-allowing models: Challenges and opportunities. *Preprints, 24th Conference on Severe Local Storms, Savannah, GA, American Meteorological Society, P12.1*.

Lang, S., W.-K. Tao, R. Cifelli, W. Olson, J. Halverson, S. Rutledge, and J. Simpson, 2007: Improving simulations of convective systems from TRMM LBA: Easterly and westerly regimes. *Journal of Atmospheric Sciences*, **64**, 1141–1164.

Lhermitte, R., 1990: Attenuation and scattering of millimeter wavelength radiation by clouds and precipitation. *Journal of Atmospheric and Oceanic Technology*, **3**, 464–479.

Lin, Y.-L., R. D. Farley, and H. D. Orville, 1983: Bulk parameterization of the snow field in a cloud model. *Journal of Applied Meteorology*, **22**, 1065–1092.

Liu, G., 2004: Approximation of single scattering properties of ice and snow particles for high microwave frequencies. *Journal of Atmospheric Sciences*, **61**, 2441–2456.

Liu, G., 2008: A database of microwave single-scattering properties for nonspherical ice particles. *Bulletin of the American Meteorological Society*, **89**, 1563–1570.

Locatelli, J. D. and P. V. Hobbs, 1974: Fall speeds and masses of solid precipitation particles. *Journal of Geophysical Research*, **79**, 2185–2197.

Marshall, J. S. and W. M. Palmer, 1948: The distribution of raindrops with size. *Journal of the Atmospheric Sciences*, **5**, 165–166.

Mlawer, E. J., S. J. Taubman, P. D. Brown, M. J. Iacono, and S. A. Clough, 1997: Radiative transfer for inhomogeneous atmosphere: RRTM, a validated correlated-k model for the long-wave. *Journal of Geophysical Research*, **102**, 16 663–16 682.

Rutledge, S. A. and P. V. Hobbs, 1983: The mesoscale and microscale structure and organization of clouds and precipitation in midlatitude cyclones. VII: A model for the seeder-feeder process in warm-frontal rainbands. *Journal of Atmospheric Sciences*, **40**, 1185–1206.

Ryan, B., 2000: A bulk parameterization of the ice particle size distribution and the optical properties in ice clouds. *Journal of Atmospheric Sciences*, **57**, 1436–1451.

Shi, J. J., et al., 2009: WRF simulations of the January 20-22 2007 snow events over eastern Canada: Comparison with in-situ and satellite observations. *Journal of Applied Meteorology and Climatology*.

Smith, P., 1984: Equivalent radar reflectivity factors for snow and ice particles. *Journal of Applied Meteorology*, **23**, 1258–1260.

Tao, W.-K., J. Shi, S. Chen, S. Lang, S.-Y. Hong, C. Peters-Lidard, S. Braun, and J. Simpson, 2008: Revised bulk-microphysical schemes for studying precipitation processes. Part I: Comparisons with other schemes. *Monthly Weather Review*.

Tao, W.-K., et al., 2003: Microphysics, radiation and surface processes in the Goddard Cumulus Ensemble (GCE) model. *Meteorology and Atmospheric Physics*, **82**, 97–137.

Twohy, C. H., A. J. Schanot, and W. A. Cooper, 1997: Measurement of condensed water content in liquid and ice clouds using an airborne counterflow virtual impactor. *Journal of Atmospheric and Oceanic Technology*, **14**, 197–202.